

From Micromagnetic to In Silico Modeling of Magnetic Nanodisks for Hyperthermia Applications

*Original*

From Micromagnetic to In Silico Modeling of Magnetic Nanodisks for Hyperthermia Applications / Manzin, Alessandra; Ferrero, Riccardo; Vicentini, Marta. - In: ADVANCED THEORY AND SIMULATIONS. - ISSN 2513-0390. - 4:5(2021). [10.1002/adts.202100013]

*Availability:*

This version is available at: 11583/2919732 since: 2021-08-31T12:27:09Z

*Publisher:*

Wiley-VCH GmbH

*Published*

DOI:10.1002/adts.202100013

*Terms of use:*

This article is made available under terms and conditions as specified in the corresponding bibliographic description in the repository

*Publisher copyright*

(Article begins on next page)

# From Micromagnetic to In Silico Modeling of Magnetic Nanodisks for Hyperthermia Applications

Alessandra Manzin,\* Riccardo Ferrero, and Marta Vicentini

Magnetic nanodisks have been recently proposed as biomedical tools for therapeutics at the nanoscale level, with a special focus on hyperthermia for cancer cure. Here we present a detailed study of permalloy nanodisks to be used in alternative to superparamagnetic iron oxide nanoparticles, as efficient heating agents that release heat via magnetic hysteresis. A micromagnetic modeling analysis is carried out to identify sizes and ac field parameters that maximize the specific loss power (SLP), guaranteeing the fulfillment of biophysical constraints (Hergt–Dutz limit) and vortex state at remanence (reduced agglomeration effects). The highest SLP ( $790 \text{ W g}^{-1}$ ) is found for 100 nm diameter and 20 nm thickness nanodisks, excited at a frequency of 75 kHz. Further analysis elucidates the influence of magnetostatic interactions and local nanodisk-field orientation on the SLP of nanodisk clusters, which originate from the deposition in target tissues. At high concentrations, magnetostatic interactions can lead to a reduction of 40–50% in the hysteresis losses. From thermal simulations, we finally demonstrate that in a murine model temperature increments comparable to that obtained in calorimetric measurements under quasi-adiabatic conditions can be achieved only by using an order of magnitude larger dosage of nanodisks, due to blood perfusion effects.

alternative to the typically used superparamagnetic iron oxide nanoparticles (SPIONs).<sup>[12,13]</sup> As an example, magnetic nano/microdisks have been proposed as efficient magneto-mechanical actuators to destroy cancer cells, exploiting their ability to rotate under the action of low frequency magnetic fields ( $f = 10\text{--}20 \text{ Hz}$ ).<sup>[14–18]</sup> They have also been studied for drug delivery and gene therapy, investigating the possibility of driving the release of drug molecules via mechanical oscillation and torque effects, induced by low frequency fields as well ( $f \cong 30 \text{ Hz}$ ).<sup>[16–20]</sup> Furthermore, attention has been focused on possible uses in cell separation from blood samples for early cancer detection,<sup>[21]</sup> and in frequency-based nanoparticle sensing, exploiting changes in the ferromagnetic resonance behavior.<sup>[22]</sup>

Another potential application is magnetic hyperthermia for cancer cure, where disk-, ring-, cylinder-, sphere-, cube-, or flower-shaped nanostructures made of different magnetic materials have been explored as heating agents for the generation

## 1. Introduction

In the last two decades, different types of magnetic nanostructures, like nanodisks that exhibit vortex configuration, have been investigated for potential use in magnetic recording, magneto-logic devices, and spin-torque nano-oscillators.<sup>[1–5]</sup> More recently, attention has been paid to biomedical applications related to nanomedicine therapeutics and diagnostics, also with the exploration of non-spherical micro- and nanoparticles,<sup>[6–11]</sup> as an

of strongly localized increments of temperature.<sup>[23–32]</sup> Under the action of ac magnetic fields ( $f \cong 50\text{--}500 \text{ kHz}$ ) and for sufficiently large size, they can produce heat via magnetic hysteresis, showing values of specific loss power (SLP) higher than those of the clinically approved SPIONs.<sup>[33–37]</sup> Moreover, they can be characterized by vortex state at remanence (e.g., for discoidal or annular shape), feature that leads to small magnetostatic interactions and, advantageously, to low probability of aggregation. However, the nanomaterial design has to be followed by a careful selection of the source excitation parameters (frequency  $f$  and amplitude  $\hat{H}_a$  of the applied magnetic field) to not exceed the upper limitation of  $5 \times 10^9 \text{ A m}^{-1} \text{ s}^{-1}$  (Hergt–Dutz limit),<sup>[38]</sup> conventionally used in the literature to avoid unwanted non-selective heating due to the generation of eddy currents. This criterion was proposed after the more rigid limitation of  $4.85 \times 10^8 \text{ A m}^{-1} \text{ s}^{-1}$ , known as the Atkinson–Brezovich limit.<sup>[39]</sup>

Despite the heating efficacy of magnetic nanomaterials with hysteresis properties, a systematic analysis is required to identify dimensional and physical properties as well as ac source conditions that maximize the SLP, guaranteeing at the same time the fulfillment of the biophysical constraints.<sup>[32]</sup> In the evaluation of the produced SLP different phenomena have to be taken into account, such as the local magnetostatic interactions and the possible reorientation with the applied field in low viscosity

A. Manzin, R. Ferrero, M. Vicentini  
Istituto Nazionale di Ricerca Metrologica (INRIM)  
Strada delle Cacce 91, Torino 10135, Italy  
E-mail: a.manzin@inrim.it  
M. Vicentini  
Politecnico di Torino  
Corso Duca degli Abruzzi 24, Torino 10129, Italy

The ORCID identification number(s) for the author(s) of this article can be found under <https://doi.org/10.1002/adts.202100013>

© 2021 The Authors. Advanced Theory and Simulations published by Wiley-VCH GmbH. This is an open access article under the terms of the Creative Commons Attribution License, which permits use, distribution and reproduction in any medium, provided the original work is properly cited.

DOI: 10.1002/adts.202100013

media. Another fundamental aspect is the determination of the temperature increase produced in biological tissues as a function of the nanomaterial dose and of the exposure time, to select operative conditions to be used in therapeutic sessions.

Here, we focus on nanodisks made of permalloy ( $\text{Ni}_{80}\text{Fe}_{20}$ ), considered instead of iron oxide to explore the possibility to obtain greater values of SLP, due to the higher saturation magnetization. Moreover, permalloy nanodisks coated on both top and bottom surface with a gold layer have shown very good biocompatibility and easy surface modification for further biofunctionalization.<sup>[40]</sup>

A parametric analysis is performed to find the optimal geometrical properties, considering the Hergt–Dutz limit<sup>[38]</sup> for the selection of  $f$  and  $\hat{H}_a$ . Specifically, we vary the disk diameter from 100 to 800 nm and the thickness from 15 to 30 nm. The SLP is derived from hysteresis losses, being the predominant heating contribution for the considered nanomaterials. The analysis is carried out via numerical modeling, calculating the hysteresis loops with a GPU-parallelized micromagnetic solver for the spatial-time integration of the Landau–Lifshitz–Gilbert (LLG) equation.<sup>[41]</sup> The influence of nanodisk local concentration is also investigated, focusing on the role of magnetostatic interactions and relative orientation with the applied field. Moreover, we analyze the mechanical behavior in media with decreasing viscosity, to verify the occurrence of a rotational motion driven by ac fields with frequency variable in a range of interest for magnetic hyperthermia.

After selecting field parameters  $f$  and  $\hat{H}_a$ , in accordance with the Hergt–Dutz limit,<sup>[38]</sup> we calculate the temperature increase in test tubes filled with ferrofluids containing permalloy nanodisks with variable concentration, under both adiabatic and non-adiabatic conditions. The analysis, carried out with a finite element model for the heat transfer equation, is focused on nanodisks with optimized hyperthermia properties, addressed by the previous micromagnetic modeling study. Then, we determine, by solving the Pennes' bioheat transfer equation, the temperature increase induced in biological tissues. The study is focused on a computational anatomical model of a mouse, changing the size of the target region, where the nanodisks are dispersed with variable dose, and its location in the body, considering different organs.

## 2. Results and Discussion

### 2.1. Influence of Size

The heating contribution due to hysteresis losses can be finely tuned by varying nanodisk geometrical properties. To this aim, we investigate the influence of nanodisk diameter  $d$  and thickness  $t$  on the magnetization reversal mechanism and hysteresis loop area, first focusing on a single nanodisk and thus disregarding magnetostatic interactions. The loops are initially calculated by applying the external field in the nanodisk plane and neglecting thermal noise, conditions that lead to the highest energy losses. We can consider the static approximation for the hysteresis loop evaluation, due to the time scale of magnetization relaxation processes at each equilibrium point, resulting in tens of nanoseconds at most (i.e., for irreversible jumps).

The micromagnetic simulations, carried out with the numerical model described in Section 4, are performed by considering magnetic properties typical of permalloy, i.e., saturation magnetization of  $860 \text{ kA m}^{-1}$ , exchange constant of  $13 \text{ pJ m}^{-1}$ , negligible magnetocrystalline anisotropy and damping coefficient of 0.02. The nanodisk diameter is varied in the range from 100 to 800 nm and the thickness from 15 to 30 nm, in order to find the optimal conditions for the maximization of the specific heating capabilities.

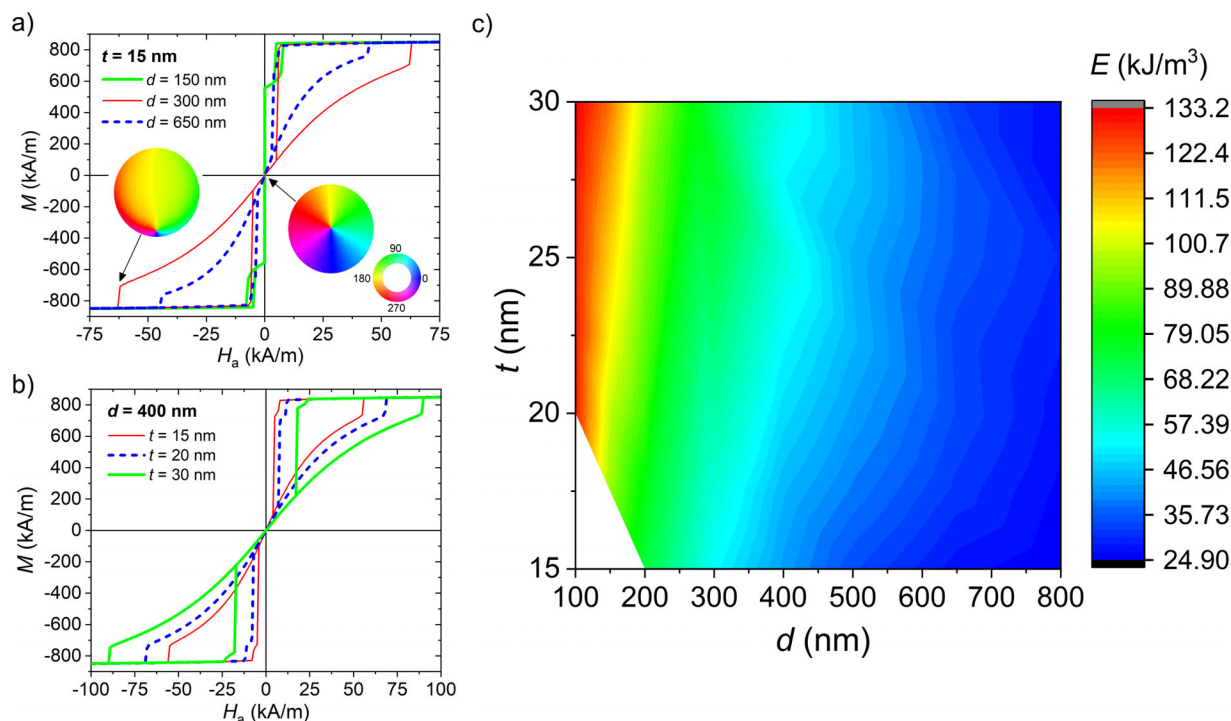
The influence of geometrical properties on the hysteresis loop shape are depicted in Figure 1a,b, which report respectively the loops calculated for different diameters ( $d = 150, 300$ , and  $650 \text{ nm}$ ) fixing  $t$  to 15 nm, and for different thicknesses ( $t = 15, 20$ , and  $30 \text{ nm}$ ) fixing  $d$  to 400 nm. Apart for the case with  $d = 150 \text{ nm}$  and  $t = 15 \text{ nm}$ , each loop branch is characterized by two irreversible jumps, corresponding to vortex nucleation and expulsion, connected through a reversible part dominated by vortex translation in the disk plane. At remanence, a negligible average magnetization is found, with the vortex pinned at the nanodisk center. The evolution of magnetic state is clearly illustrated by the magnetization maps reported in Figure 1a, calculated for  $d = 300 \text{ nm}$  and  $t = 15 \text{ nm}$ . When  $d = 150 \text{ nm}$  and  $t = 15 \text{ nm}$ , the magnetization reversal occurs at zero applied field with an irreversible jump between two C-states, leading to a negligible loop area.

Figure 1a,b well demonstrate that, in the case of vortex formation, wider hysteresis loops can be obtained by reducing nanodisk diameter and/or increasing nanodisk thickness. These conditions lead to greater heating capabilities, as shown by the diagram in Figure 1c, which reports the specific energy losses,  $E = \mu_0 \oint \mathbf{H}_a \cdot d\mathbf{M}$ , calculated from the major hysteresis loops as a function of parameters  $d$  and  $t$ . The data are plotted only for the cases characterized by vortex nucleation, confirming, for the considered values of  $d$  and  $t$ , the classification of remanent states previously reported by Ha et al.<sup>[42]</sup>

To maximize the hysteresis losses, the amplitude of the external field should be large enough to enable vortex expulsion. For the major loops, the estimated losses vary from  $25 \text{ kJ m}^{-3}$  (case with  $d = 800 \text{ nm}$  and  $t = 15 \text{ nm}$ ) to  $133 \text{ kJ m}^{-3}$  (case with  $d = 100 \text{ nm}$  and  $t = 30 \text{ nm}$ ). For the considered geometrical properties, it is worth noting that vortex expulsion can be obtained by applying external fields with large amplitudes, ranging from  $\approx 63 \text{ kA m}^{-1}$  for  $d = 800 \text{ nm}$  and  $t = 15 \text{ nm}$  up to  $\approx 122 \text{ kA m}^{-1}$  for  $d = 150 \text{ nm}$  and  $t = 30 \text{ nm}$ . This strongly impacts on the maximum field frequency that can be selected to guarantee the satisfaction of the biophysical constraints for safe in vivo treatments.

### 2.2. Influence of Temperature

It should be remarked that the results reported in Figure 1 have been calculated by neglecting thermal noise and by assuming ideal material and geometrical properties (absence of defects) for the considered nanodisks. If we include thermal agitation effects, introduced in the simulations via a Langevin approach (see Section 4), we can observe a modification of the hysteresis loop, with a significant decrease in the field corresponding to vortex expulsion and, consequently, in the saturation field. Thermal noise can



**Figure 1.** Role of geometrical properties. a) Comparison of the hysteresis loops calculated for different diameters ( $d = 150, 300$ , and  $650$  nm) fixing thickness  $t$  to  $15$  nm. The maps show the magnetization configurations at remanence and at the equilibrium state immediately before vortex expulsion (the color wheel represents the angle, in degrees, between the magnetization vector and the x-axis). b) Comparison of the hysteresis loops calculated for different thicknesses ( $t = 15, 20$ , and  $30$  nm) fixing diameter  $d$  to  $400$  nm. c) Diagram reporting the specific energy losses, estimated as a function of  $d$  ( $100$ – $800$  nm) and  $t$  ( $15$ – $30$  nm), neglecting thermal noise effects. The white area corresponds to no vortex nucleation conditions.

moderately impact also on the vortex nucleation field, which can be randomly reduced or amplified.

The influence of temperature on the hysteresis loops is illustrated in **Figure 2a**, for nanodisks with a thickness of  $30$  nm and a diameter variable from  $150$  to  $500$  nm. Each new loop has been calculated by setting the temperature at  $45$  °C ( $318$  K), a value that is expected to be reached during hyperthermia sessions, and by extracting the average curves over 20 stochastic realizations; anyway, taking into account the randomness of thermal fluctuations we can expect practically negligible variations in the magnetization reversal process by varying the temperature within a limited range. The saturation magnetization  $M_s$  at  $318$  K has been fixed to  $800$  kA m $^{-1}$ , according to the law  $M_s(T) = M_{s_0}(1 - bT^{3/2} - cT^{5/2} - aT^2)$  derived from the classical spin-wave theory,<sup>[43,44]</sup> considering  $M_{s_0} = 860$  kA m $^{-1}$ ,  $a = 0.19 \times 10^{-7}$  K $^{-2}$ ,  $b = 0.88 \times 10^{-5}$  K $^{-3/2}$ , and  $c = 0.09 \times 10^{-7}$  K $^{-5/2}$ .<sup>[44]</sup>

Figure 2b compares the values of the vortex expulsion field  $H_{exp}$  determined with and without the inclusion of thermal effects, for the entire considered ranges of thickness and diameter. It is worth noting that the role of temperature is higher for the nanodisks with smaller diameter and larger thickness, and reduces with the diameter increase. The highest expulsion field,  $122$  kA m $^{-1}$ , obtained with zero temperature when  $d = 150$  nm and  $t = 30$  nm, decreases up to  $88.5$  kA m $^{-1}$ . As a conclusion, thermal effects favor the vortex expulsion enabling to reach saturation with strongly reduced fields. Anyway, the impact on the hysteresis losses is quite limited, with a decrease in the order of  $24$ – $30\%$ , for example, for the major loops, the estimated losses

vary from  $19$  kJ m $^{-3}$  (against  $25$  kJ m $^{-3}$  when  $d = 800$  nm and  $t = 15$  nm) to  $93$  kJ m $^{-3}$  (against  $133$  kJ m $^{-3}$  when  $d = 100$  nm and  $t = 30$  nm).

If we consider the Hergt–Dutz limit<sup>[38]</sup> and the applied field is in the order of the vortex expulsion field, the maximum allowable frequency  $f_{max}$  should vary in the range  $55$ – $160$  kHz (Figure 2c, top). The lowest values of frequencies have to be selected for the excitation of nanodisks with small diameter and thickness of  $20$ – $30$  nm. Despite the reduction in frequency due to the fulfillment of the biophysical constraint, these nanodisks result to be the most efficient in terms of heat generation, as illustrated by the diagram in Figure 2c (bottom), which reports the maximum obtainable specific loss power ( $SLP_{max}$ ) as a function of  $d$  and  $t$ , calculated by fixing the frequency to  $f_{max}$ . The SLP estimation is performed by setting the mass density of permalloy at  $8.72$  g cm $^{-3}$ . In particular,  $SLP_{max}$  varies from  $790$  W g $^{-1}$  ( $d = 100$  nm,  $t = 20$  nm) to  $235$  W g $^{-1}$  ( $d = 800$  nm,  $t = 30$  nm), when applying an external field with a frequency of  $75$  and  $100$  kHz, respectively. This is a very satisfying result, considering that the  $100$  nm size, for which the largest SLP is obtained, is also more beneficial in terms of cell uptake, blood circulation half-life and biodistribution.<sup>[45]</sup> Moreover, the achieved heating performance are better or comparable to the ones previously documented for iron oxide nanodisks. For the latter an SLP of  $125$  W g $^{-1}$  was reported for diameters larger than  $20$  nm, setting the field frequency  $f$  at  $310$  kHz and its amplitude  $\hat{H}_a$  at  $64$  kA m $^{-1}$ ,<sup>[45]</sup> while an SLP of about  $250$  W g $^{-1}$  was found for  $150$ – $200$  nm diameters, with  $f = 180$  kHz and  $\hat{H}_a = 0.95$  kA m $^{-1}$ .<sup>[46]</sup> An

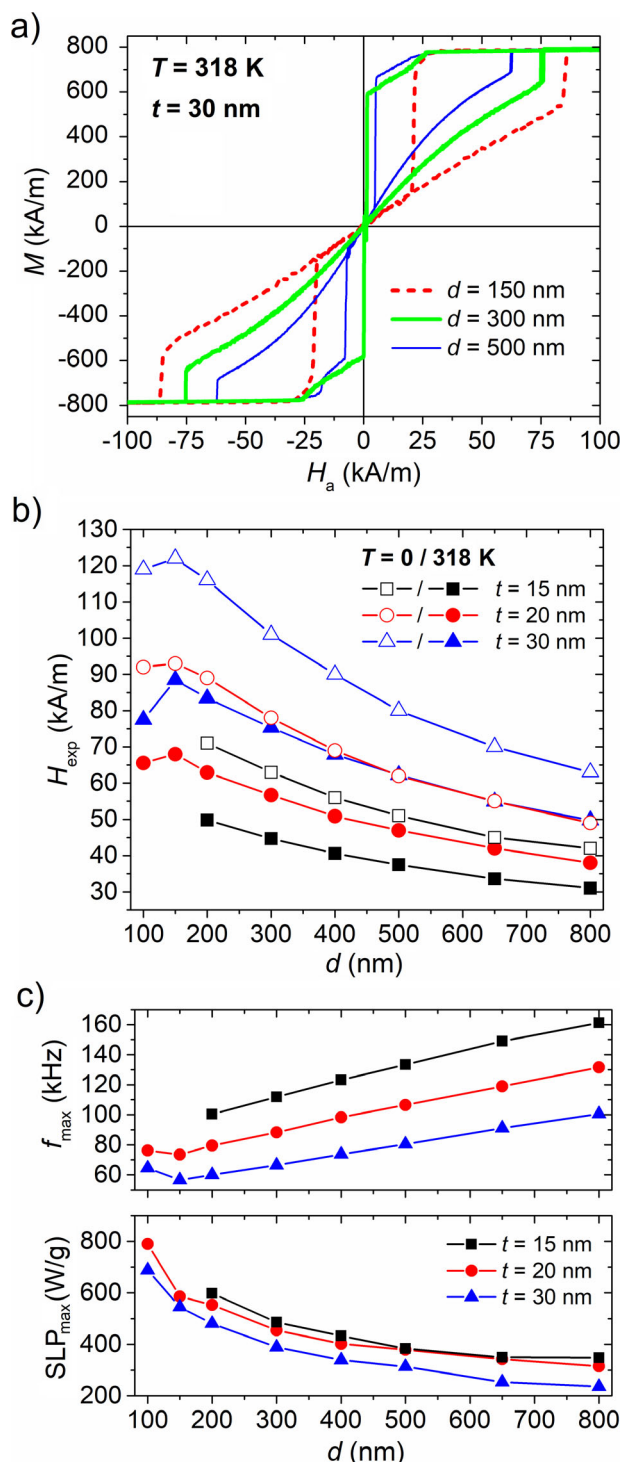


**Figure 2.** Role of temperature. a) Comparison of the hysteresis loops calculated for different diameters ( $d = 150, 300$ , and  $500$  nm) and thickness  $t$  equal to  $30$  nm by including thermal noise ( $T = 318$  K). b) Influence of thermal noise on vortex expulsion fields for different values of  $d$  ( $100$ – $800$  nm) and  $t$  ( $15$ – $30$  nm). c) Maximum frequency  $f_{\max}$  (top) and specific loss power  $SLP_{\max}$  (down) as a function of  $d$  and  $t$  when including thermal noise and considering Hergt–Dutzy limit.

impressive value of SLP, in the range of  $4400 \text{ W g}^{-1}$  was also reported for  $225$  nm diameter iron oxide nanodisks,<sup>[26]</sup> but it was obtained under the application of a field with  $f = 488$  kHz and  $\hat{H}_a = 47.8 \text{ kA m}^{-1}$ , thus exceeding the Hertz–Dutzy limit of about five times. Moreover, the larger nanodisk size ( $225$  nm against  $100$  nm) can negatively impact on the internalization by cancerous cells and on the average lifetime in blood.<sup>[45]</sup>

### 2.3. Influence of Disk-Field Relative Orientation and Dispersion Medium

The previous results have been obtained by applying the external field in the nanodisk plane. In a real hyperthermia session, the nanodisks are dispersed in the target biological tissue with a stochastic spatial distribution. Thus, the relative orientation between the external applied field and each nanodisk is different, impacting on the magnetization reversal process and, consequently, on the global hysteresis losses. Here, we investigate the role of the inclination of the applied field with respect to the nanodisk plane, evaluating the vortex nucleation and vortex expulsion fields,  $H_{\text{nuc}}$  and  $H_{\text{exp}}$ , as a function of disk-field relative angular orientation  $\varphi$  (see the schematic below **Figure 3a** for its definition), also including temperature effects ( $T = 318$  K). We focus the attention on a nanodisk with  $d = 150$  nm and  $t = 25$  nm, dimensions that guarantee vortex nucleation and enable us to obtain good hyperthermia properties, as illustrated by the diagram in **Figure 1c**.

As an example, **Figure 3a** shows the hysteresis loop calculated when  $\varphi = 70^\circ$ ; the modification of the loop shape with respect to the case  $\varphi = 0$  is well evident, with a strong amplification of the vortex expulsion field, which reaches values in the order of  $180 \text{ kA m}^{-1}$ . The results obtained when varying  $\varphi$  between  $0$  and  $85^\circ$  are summarized in **Figure 3b**, which highlights how the increase in  $\varphi$  leads to an amplification of both  $H_{\text{nuc}}$  and  $H_{\text{exp}}$ . In particular,  $H_{\text{nuc}}$  varies moderately when  $\varphi$  is in the range of  $0$ – $40^\circ$ , with a steep rise for values of  $\varphi$  larger than  $80^\circ$ , due to the reduction in the applied field component lying in the nanodisk plane. In particular, the simulations provide for  $H_{\text{nuc}}$  an estimate of  $\approx 230 \text{ kA m}^{-1}$  when  $\varphi = 85^\circ$ .

Also the vortex expulsion field  $H_{\text{exp}}$  increases smoothly up to  $\varphi = 40^\circ$ , but reaches a value close to  $400 \text{ kA m}^{-1}$  when  $\varphi = 85^\circ$ , resulting in a quasi-infinite amplitude if the external field is applied orthogonally to the nanodisk plane and thermal effects are disregarded. This makes critical the generation of hysteresis losses (presence of a loop with non-negligible area) under real operative conditions, which have to be governed by biophysical constraints on the maximum allowable applied field amplitude and frequency. For the specific dimensions of  $d = 150$  nm and  $t = 25$  nm, if we fix  $\hat{H}_a$  to  $100 \text{ kA m}^{-1}$  and  $f$  to  $50$  kHz to guarantee the satisfaction of Hergt–Dutzy limit, a nanodisk that is orientated with an angle  $\varphi$  higher than  $45^\circ$  with respect to the field provides a negligible contribution to the global hysteresis losses. In this case, after the application of the alternating field, the vortex (present at the initial remanence state) starts to move reversibly in the nanodisk plane, without generating losses, due to the absence of cyclical vortex expulsion and nucleation. This has a negative impact on the total amount of heat that can be produced by a stochastic



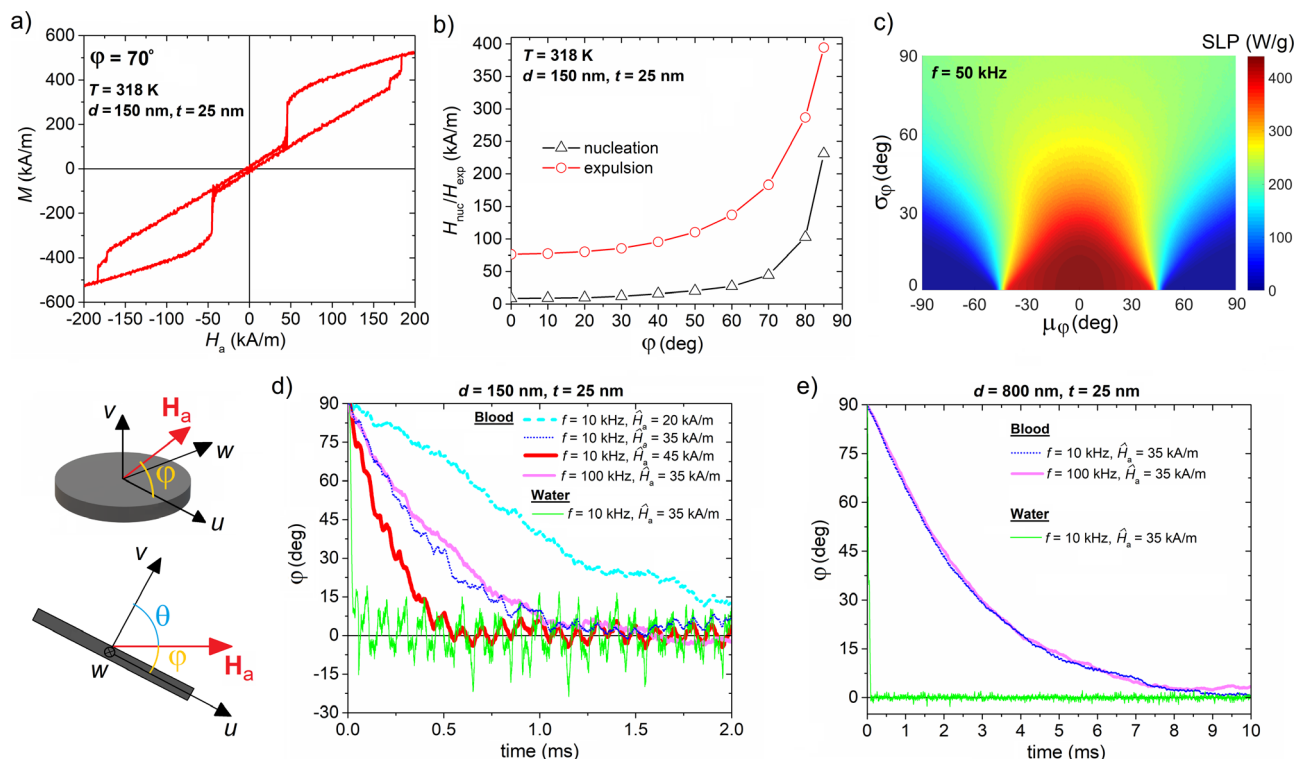


**Figure 3.** Role of disk-field relative orientation and dispersion medium. a) Hysteresis loop of a nanodisk with diameter  $d = 150$  nm and thickness  $t = 25$  nm, calculated for an external field applied at an angle  $\varphi = 70^\circ$  with respect to the nanodisk plane (see schematic below), including thermal effects ( $T = 318$  K). b) Vortex nucleation and expulsion fields for the same nanodisk as a function of disk-field relative angular orientation  $\varphi$ . c) Diagram of the SLP of random distributions of 10 000 nanodisks ( $d = 150$  nm,  $t = 25$  nm) with angular orientation governed by a Gaussian function having mean  $\mu_\varphi$  and standard deviation  $\sigma_\varphi$  (the field frequency is set at 50 kHz). d) Time-evolution of the disk-field relative orientation  $\varphi$ , as a function of applied field parameters and dispersion fluid (water or blood), for a nanodisk with (d) ( $d = 150$  nm,  $t = 25$  nm) and (e) ( $d = 800$  nm,  $t = 25$  nm).

spatial distribution of nanodisks dispersed in a target tissue, as well illustrated by the diagram in Figure 3c. In particular, Figure 3c reports the SLP extracted from a Monte Carlo simulation of random distributions of 10 000 non-interacting nanodisks (infinite dilution) with variable angular orientation  $\varphi$  governed by a Gaussian function having mean  $\mu_\varphi$  and standard deviation  $\sigma_\varphi$ . The results are obtained for nanodisks with  $d = 150$  nm and  $t = 25$  nm, setting  $\hat{H}_a$  at  $100 \text{ kA m}^{-1}$  and  $f$  at 50 kHz. Values of SLP between  $300$  and  $440 \text{ W g}^{-1}$  can be found when most of the nanodisks have angular orientation  $\varphi$  lower than  $40^\circ$ , while negligible hysteresis losses are obtained when almost all the nanodisks are tilted of angles larger than  $60^\circ$ . The average is around  $225 \text{ W g}^{-1}$ , which provides an approximated estimate of the amount of heat that could be deposited in a real hyperthermia session.

A phenomenon that has to be considered is the possible rotation of the nanodisks within the medium in which they are dispersed, to align themselves with the applied field. This effect is here analyzed by means of a simple physical model, which takes into account the viscous drag torque and thermal fluctuations, focusing on fluids with viscosity properties similar to that of water and blood (see Section 4). Inside high-viscosity media (e.g., biological tissues and stiff gelatin gels), we can assume that the nanodisks are immobilized.<sup>[25,47]</sup>

The rotational dynamics of a nanodisk with  $d = 150$  nm and  $t = 25$  nm is shown in Figure 3d, which reports the time-evolution of the disk-field relative orientation  $\varphi$  under different operative

conditions, depending on the applied field amplitude ( $20$ – $45 \text{ kA m}^{-1}$ ) and frequency ( $10$ – $100 \text{ kHz}$ ), and on the dispersion fluid (water or blood). The fluid viscosity is fixed to  $0.894 \text{ mPa}\cdot\text{s}$  for water (at environment temperature) and to  $58 \text{ mPa}\cdot\text{s}$  for blood at low shear rate.<sup>[48]</sup> At the beginning of the transient, the nanodisk is assumed to be orthogonal to the field and in vortex state. When the field is applied, the vortex starts to oscillate in the disk plane trying to follow the field variations. In water, the alignment with the field is practically instantaneous and a small amplitude oscillatory behavior appears, governed by Brownian effects. In blood, the motion is slower and the nanodisk completes its rotation in a time interval in the order of  $0.5$ – $2$  ms, depending on  $\hat{H}_a$ . The increase in the field amplitude leads to a reduction in the time required for the alignment, due to the more pronounced displacement of the vortex in the nanodisk plane, responsible for the generation of a more significant torque. In particular, when varying  $\hat{H}_a$  from  $20$  to  $45 \text{ kA m}^{-1}$  there is a halving of the alignment time, while negligible variations are found when modifying the frequency. The obtained results demonstrate that in fluids the alignment with the field can be achieved even for very low values of  $\hat{H}_a$ , despite the inability to magnetically saturate the nanodisks and the generation of a very small torque on the out-of-plane vortex magnetization component.

For larger nanodisk dimensions (e.g.,  $d = 800$  nm and  $t = 25$  nm), the time needed for the complete rotation increases, reaching a value in the order of  $10$  ms when  $\hat{H}_a = 35 \text{ kA m}^{-1}$

(see Figure 3e). Anyway, also in this case the reorientation of the nanodisks with the field occurs in a very short time window, leading to a condition for which the SLP is maximized, as proven by Figure 3c. This further corroborates the experimental results previously obtained on magnetite ellipsoidal nanoparticles<sup>[25]</sup> and nanodisks,<sup>[26]</sup> for which an enhancement of the heating efficiency has been observed in aqueous suspensions with respect to gel media.

## 2.4. Role of Local Concentration and Magnetostatic Interactions

The extravasation and accumulation of nanomaterials in tumor tissues are not completely understood phenomena governed by both inter-endothelial and trans-endothelial transport processes. Inter-endothelial routes comprise pores or open fenestrations in the tumor blood vessels, while trans-endothelial pathways are based on transcytosis by tumor endothelial cells.<sup>[49–51]</sup> As corroborated by micro-CT imaging, high-resolution optical imaging and numerical modeling, the spatial-temporal distribution of nanomaterials in the target tissue is not uniform, with the formation of high-density agglomerates imposed by the host biological matrices,<sup>[52–56]</sup> as simplified in the schematic of Figure 4a. This effect can be amplified in the presence of magnets with collecting action<sup>[57]</sup> and, in the case of magnetic hyperthermia, it can lead to a heat deposition variable in space and in time and, consequently, to a heterogeneous temperature increase. The heat released in the tissue results to be a function of the local concentration of the magnetic nanomaterials, with the SLP locally influenced by the magnetostatic interactions and the orientation with respect to the applied field. As elucidated in Sub-section 2.3 the latter plays an important role in the case of nanodisks, due to their shape anisotropy properties.

To investigate the influence of magnetostatic interactions, we calculate the magnetization reversal processes and hysteresis losses of an ensemble of 55 nanodisks (with 150 nm diameter and 25 nm thickness), randomly distributed in the space with different volume concentrations. The volume concentration is defined as the ratio  $V_{\text{nanodisks}}/V_{\text{system}}$ , where  $V_{\text{nanodisks}}$  is the volume of a nanodisk multiplied by the number of nanodisks and  $V_{\text{system}}$  is the minimum volume of the 3D domain containing all the nanodisks. To limit the effect of orientation with respect to the field, all the considered stochastic distributions are characterized by a variable angle  $\varphi$  governed by a Gaussian function having mean  $\mu_{\varphi}$  in the order of 10–15°.

The influence of nanodisk volume concentration on the local SLP is shown in Figure 4a, for a field frequency of 50 kHz. The increase in volume concentration leads to a decrease in the SLP, which reduces from  $\approx 440 \text{ W g}^{-1}$  for well-dispersed systems, characterized by negligible magnetostatic interactions, to  $\approx 260 \text{ W g}^{-1}$  for concentrations close to 30%. This means that the heat (joules) released for a concentration of 30% is only 60% of the amount that could be achieved if the SLP did not decay with concentration rise. This result corroborates previous findings on the detrimental effect of magnetostatic interactions on the hyperthermia properties of magnetic nanomaterials, documented by simulations<sup>[58]</sup> as well as measurements in liquids with variable ferrofluid concentration.<sup>[31,59]</sup>

The reduction in the hysteresis loop area with volume concentration is described by Figure 4b, which shows a compari-

son between the hysteresis loops calculated at  $T = 318 \text{ K}$  for two concentrations, equal to 0.1% and 27.6%. The low concentration gives rise to a loop with two well-defined irreversible jumps, corresponding to vortex nucleation and expulsion, phenomena that occurs in a synchronous way in all the nanodisks. The high concentration is responsible for a gradual reversal process, with indistinguishable vortex nucleation/expulsion transitions. This is a consequence of the strong magnetostatic interactions between nanodisks and of the local misalignment with the applied field, which lead to a non-synchronous magnetization switching with vortices generated and expelled at different applied fields. The above effect is well illustrated by the maps of the magnetization spatial distributions, calculated at different equilibrium points along the reversal process (Figure 4c). It is clear that for high concentrations not all the nanodisks are in the vortex configuration at remanent state, with the appearance of non-negligible remanence magnetization and coercive field.

## 2.5. Thermal Effects in Test Tubes

Typically, the heating properties of magnetic nanomaterials are tested by performing calorimetric measurements of suspensions in in vitro tissue analogues, which can be aqueous solutions or gels. A critical issue is the setup of adiabatic conditions, to avoid heat transfer between the ferrofluid sample and the surroundings, and thus minimize external environment effects. To investigate the impact of non-adiabatic conditions, we calculate the time-evolution of temperature within test tubes filled with ferrofluids containing different concentrations of permalloy nanodisks having a diameter of 150 nm and a thickness of 25 nm. The used numerical model is described in Section 4.

To simulate different environmental cooling conditions (free convection in air), a heat transfer coefficient variable from 0 to  $50 \text{ W m}^{-2} \text{ K}^{-1}$  is considered at the interface between the tube exterior surface and the surrounding air. The tube, made of propylene (material density  $\rho$  of  $905 \text{ kg m}^{-3}$ , heat capacity  $C_p$  of  $1900 \text{ J kg}^{-1} \text{ K}^{-1}$ , thermal conductivity  $k$  of  $0.185 \text{ W m}^{-1} \text{ K}^{-1}$ ), has an internal diameter of 6.1 mm at the beginning of the non-tapered part, a total height of 3 cm and a wall thickness of 0.6 mm. The tube is partially filled by the ferrofluid, i.e., up to 1.75 cm from the tapered bottom.

Figure 5a shows the spatial distribution of the temperature increase at the end of the heating transient, consequent to the application of a uniform 50 kHz magnetic field; the nanodisks are dispersed in water ( $\rho = 997.05 \text{ kg m}^{-3}$ ,  $C_p = 4183 \text{ J Kg}^{-1} \text{ K}^{-1}$ ,  $k = 0.6 \text{ W m}^{-1} \text{ K}^{-1}$ ) with a concentration of  $0.2 \text{ mg ml}^{-1}$ . As a first approximation, the SLP in water is set at  $440 \text{ W g}^{-1}$ , value obtained under the hypotheses of infinite dilution (optimal dispersion) and nanodisks aligned with the applied field, thanks to the low viscosity of water (see Sub-section 2.3). The map in Figure 5a, calculated for  $h = 10 \text{ W m}^{-2} \text{ K}^{-1}$ , puts in evidence how also at equilibrium, reached after  $\approx 30 \text{ min}$ , there is a temperature gradient within the ferrofluid, with a variation of  $\approx 2 \text{ K}$  between the peak (at the sample surface) and the minimum (at the tube bottom). Other effects that concur to temperature inhomogeneity comprise the magnetic field non-uniformity, convective currents, and non-uniform distribution of nanomaterials within the tube, due to precipitation toward the bottom.

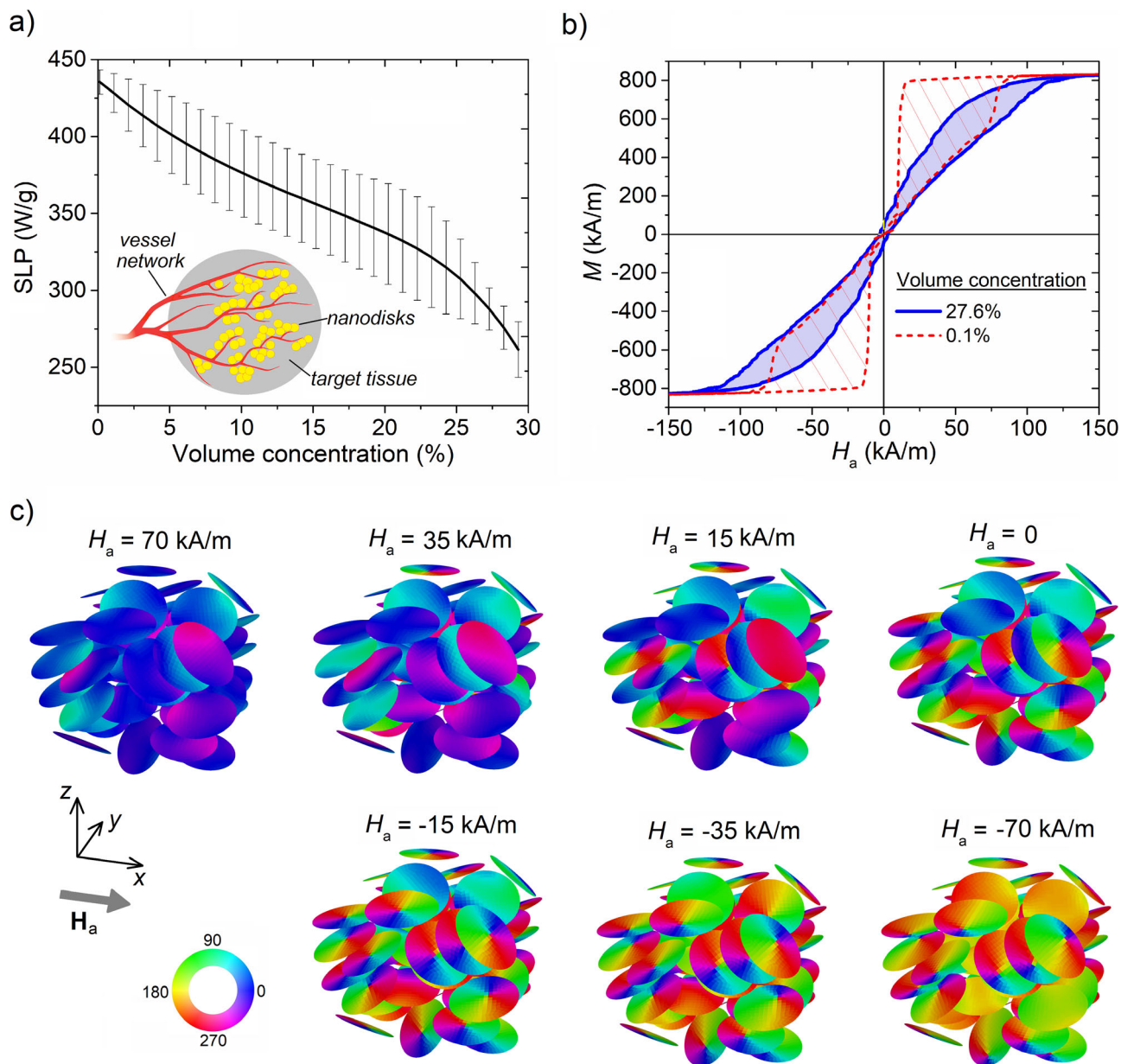


**Figure 4.** Role of local concentration and magnetostatic interactions. a) SLP versus local volume concentration, evaluated at 50 kHz for random distributions of 55 nanodisks with 150 nm diameter and 25 nm thickness, including thermal effects. The reported data represent the average of 10 stochastic realizations with the relative standard deviations; the schematic illustrates the nanomaterial release and cluster formation in tissues. b) Comparison of the hysteresis loops calculated at  $T = 318$  K for two volume concentrations, equal to 0.1% and 27.6%. c) Evolution of the equilibrium states along the descending branch of the hysteresis loop for the concentration of 27.6%. The color wheel represents the angle, in degrees, between the magnetization component in the  $xy$ -plane and the  $x$ -axis (direction of application of the field).

All these issues would require a careful location of the thermal probe within the sample or the multiple recording of heating curves placing probes at different locations in the sample holder.<sup>[60–62]</sup>

The heating transient in water, consequent to the ac field application for 25 min, and the successive cooling transient are shown in Figure 5b, as a function of parameter  $h$ , considering a nanodisk concentration of  $0.2 \text{ mg ml}^{-1}$ . The time-evolution of the temperature increase is calculated in a point internal to the sample (labeled as P in Figure 5a); at the end of the heating process

this ranges from  $2.3^\circ\text{C}$  (for  $h = 50 \text{ W m}^{-2} \text{ K}^{-1}$ ) up to  $22^\circ\text{C}$  (for adiabatic conditions), with a steeper rise for low values of  $h$ , as depicted by the summary graph on the right. It is important to note that after 25 min, the ferrofluid has not reached the regime condition yet for values of  $h$  lower than  $10 \text{ W m}^{-2} \text{ K}^{-1}$ , with the possibility of an additional increase in temperature for longer heating processes. For such values, also the considered cooling process of 25 min is not sufficient to completely cool-down the sample, with a strong rise in the transient time interval for adiabatic conditions.



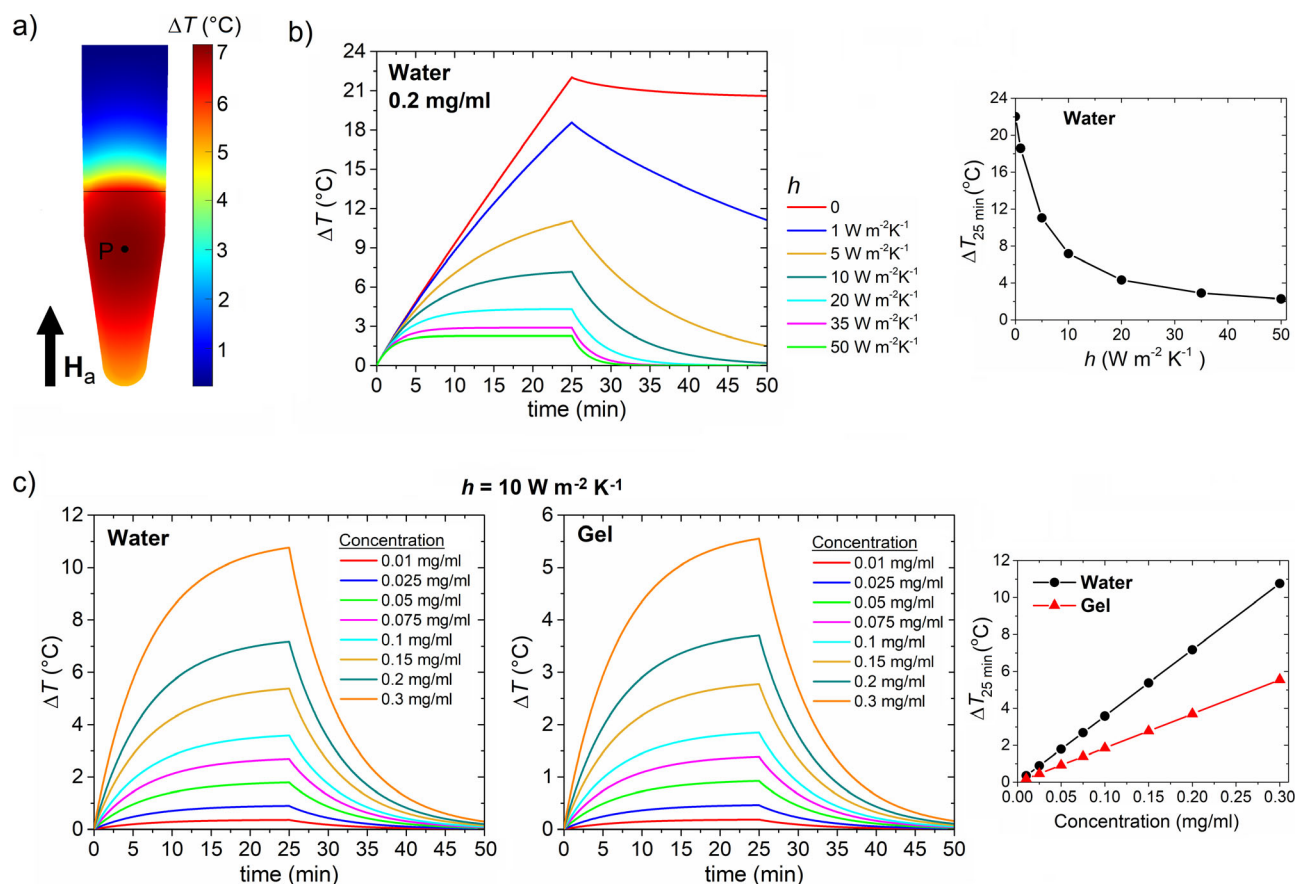


**Figure 5.** Analysis of thermal effects in test tubes. a) Map of temperature increase  $\Delta T$  at the end of the heating transient, consequent to the excitation of 150 nm diameter and 25 nm thickness permalloy nanodisks, dispersed in water with a concentration of  $0.2 \text{ mg ml}^{-1}$ . The internal black line represents the sample surface (filling level). b) Influence of the heat transfer coefficient  $h$  at the interface between air and tube wall on the heating-cooling transients in water. The temperature increase is evaluated in point P for a concentration equal to  $0.2 \text{ mg ml}^{-1}$ ; the graph on the right reports the values of  $\Delta T$  after 25 min versus  $h$ . c) Comparison of heating-cooling transients, calculated in water and gel for a concentration ranging from 0.01 to  $0.3 \text{ mg ml}^{-1}$ , fixing  $h$  to  $10 W m^{-2} K^{-1}$ ; the graph on the right reports the values of  $\Delta T$  after 25 min versus the concentration.

In Figure 5c we compare the heating-cooling transients calculated for different concentrations of nanodisks (variable from  $0.01$  to  $0.3 \text{ mg ml}^{-1}$ ), fixing  $h$  to  $10 W m^{-2} K^{-1}$  and considering as a dispersion medium both water and a viscous gel with the properties of gellan gum ( $\rho = 1010 \text{ kg m}^{-3}$ ,  $C_p = 4160 \text{ J Kg}^{-1} K^{-1}$ ,  $k = 0.53 \text{ W m}^{-1} K^{-1}$ ). For the latter, according to the analysis in Sub-section 2.3, the SLP is set at  $225 \text{ W g}^{-1}$ , due to the random orientation of the nanodisks with respect to the applied field. After a 25 min heating process, the temperature increase in point P is equal to  $10.8^\circ\text{C}$  in water and  $5.5^\circ\text{C}$  in gel, for a nanodisk concentration of  $0.3 \text{ mg ml}^{-1}$ , while an increase lower than  $0.5^\circ\text{C}$  is found in both media for a concentration of  $0.01 \text{ mg ml}^{-1}$ . The temperature variation with the concentration is linear, as depicted by the summary graph on the right.

## 2.6. Thermal Effects in a Murine Model

In this Sub-section we mimic in vivo tests, calculating the temperature increase induced in a murine model. As a first approximation, the permalloy nanodisks are uniformly dispersed in a spherical region internal to the body and then excited by a uniform ac

magnetic field along the mouse body axis. The used numerical model is described in Section 4. The role of various parameters is investigated, namely the nanodisk concentration, the size  $\delta$  of the region where the nanodisks are dispersed and that represents the target tissue, and the thermal properties of the organ where this region is mainly located. The considered murine model, depicted in Figure 6a, is a male nude normal mouse with a length of  $8.6 \text{ cm}$  (excluding tail),<sup>[63]</sup> segmented into voxels of  $0.25 \text{ mm}$  size, in turn discretized into 6 tetrahedral elements, for a total of about 9 million tetrahedrons. The tissue density and thermal properties are extracted from the IT'IS Foundation database<sup>[64]</sup> (Table 1) and the heat convection coefficient  $h$  at the air-skin interface is assumed equal to  $0.5 W m^{-2} K^{-1}$ ,<sup>[65]</sup> fixing the temperature of air to  $25^\circ\text{C}$  and the initial temperature of skin to  $33^\circ\text{C}$ .<sup>[66]</sup>

To perform a direct comparison to experiments in test tubes, we focus on the same nanodisk geometrical properties considered in Sub-section 2.5. The SLP is set at  $225 \text{ W g}^{-1}$ , chosen as a precautionary value to take into account the reduction in SLP occurring at high concentrations (Figure 4a) and when the nanodisks are dispersed in strong viscosity media, like, biological matrices, where the reorientation with the applied field is very limited (Figure 3c).

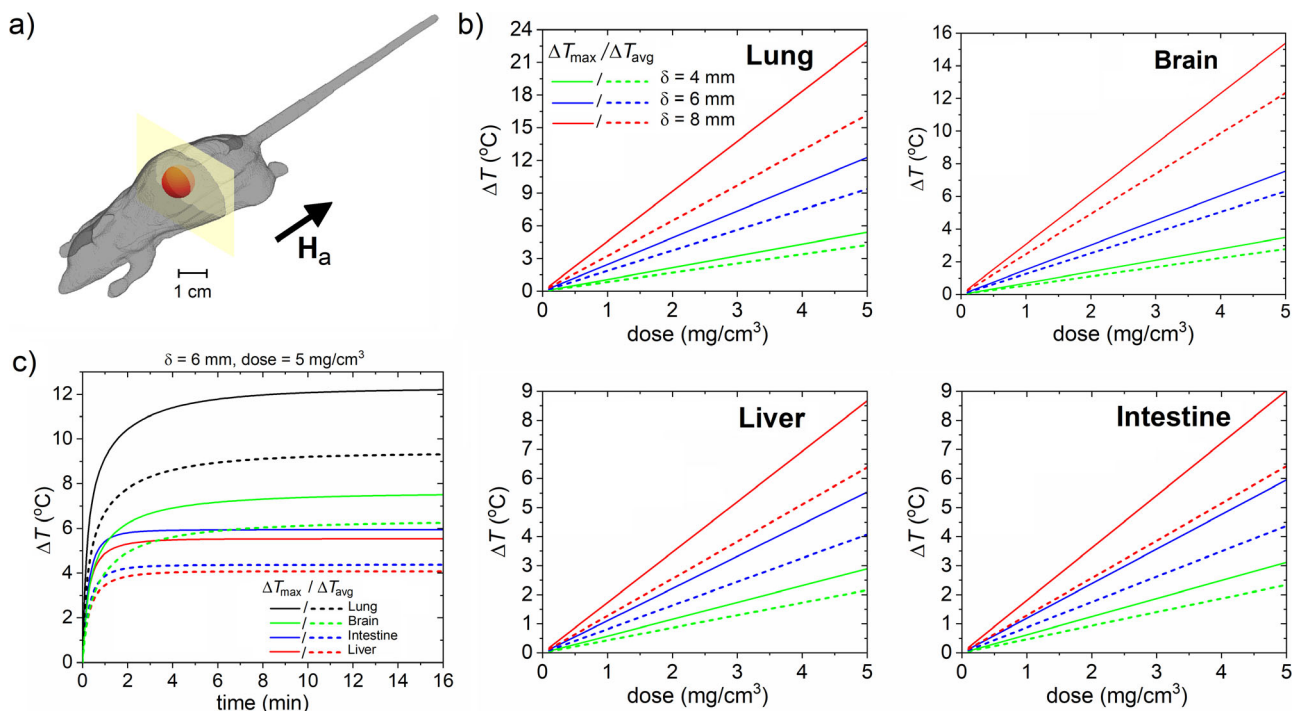


**Figure 6.** Analysis of thermal effects in a murine model. a) Schematic of the considered mouse, with the indication of the spherical region where the nanodisks are dispersed and the transversal plane for the calculation of the temperature increase map. b) Comparison of maximum and average temperature increments achieved at the heating equilibrium, by varying the organ where the target region is placed, its size  $\delta$  and the dose of permalloy nanodisks. c) Heating transients for different organs, fixing  $\delta$  to 6 mm and the nanodisk dose to 5 mg cm<sup>-3</sup>.

**Table 1.** Density and thermal properties of some of the tissues relevant for our study (Source: IT'IS Foundation database)<sup>[64]</sup>.

Tissue	Density $\rho$ [kg m <sup>-3</sup> ]	Thermal conductivity $k$ [W m <sup>-1</sup> K <sup>-1</sup> ]	Heat capacity $C_p$ [J kg <sup>-1</sup> K <sup>-1</sup> ]	Tissue-blood perfusion rate $W$ [kg s <sup>-1</sup> m <sup>-3</sup> ]	Metabolic heat generation rate $Q_m$ [W m <sup>-3</sup> ]
Lung	394	0.387	3886	2.764	2446.41
Brain	1045	0.547	3696	13.956	16 230.62
Liver	1079	0.519	3540	16.24	10 712.89
Intestine	1030	0.493	3595	18.494	16 370.23
Heart	1081	0.558	3686	19.403	42 640.2
Fat	911	0.212	2348	0.521	461.48
Thorax/Skull	1908	0.32	1313	0.334	295.49
Skin	1109	0.372	3391	2.064	1827.1

Figure 6b shows the maximum temperature increase reached at thermal equilibrium, as a function of permalloy nanodisk dose (magnetic material concentration variable between 0.1 and 5 mg per 1 cm<sup>3</sup> of tissue) and parameter  $\delta$  (ranging from 4 to 8 mm, for a volume of the target region between 34 and 268 mm<sup>3</sup>). The simulations are performed placing the target region in different organs (liver, intestine, lung, and brain). As a comparison, we also report the values of  $\Delta T$  averaged on the region itself. The temperature variation is calculated considering as a reference the thermal gradient due to the only metabolic heat.

It is important to note that for the lowest nanodisk dose (0.1 mg cm<sup>-3</sup>), due to the dominance of blood perfusion effects, the temperature increase is practically negligible, regardless of  $\delta$  and the target organ, while for the same concentration in water or

in a viscous gel this results to be 3.6 and 1.9 °C, respectively (see Sub-section 2.5). To observe an appreciable rise in temperature in the perfused biological tissues, a larger amount of magnetic material is needed, in line with previous findings.<sup>[47,67–69]</sup> As an example, when  $\delta = 4$  mm, a dose of at least 5 mg cm<sup>-3</sup> is required to obtain a maximum increase of some degrees centigrade (i.e., 2.9 °C in the liver, 3.1 °C in the intestine, 3.5 °C in the brain, and 5.4 °C in the lung). When doubling the size of the spherical region where the nanodisks are dispersed there is a significant increase in the maximum temperature increment, which ranges from 8.7 °C in the liver to 22.9 °C in the lung, reaching temperatures compatible with thermal ablation.<sup>[47]</sup> This result demonstrates the possibility of reducing the nanodisk dose for larger tissue portions, with a consequent limitation of

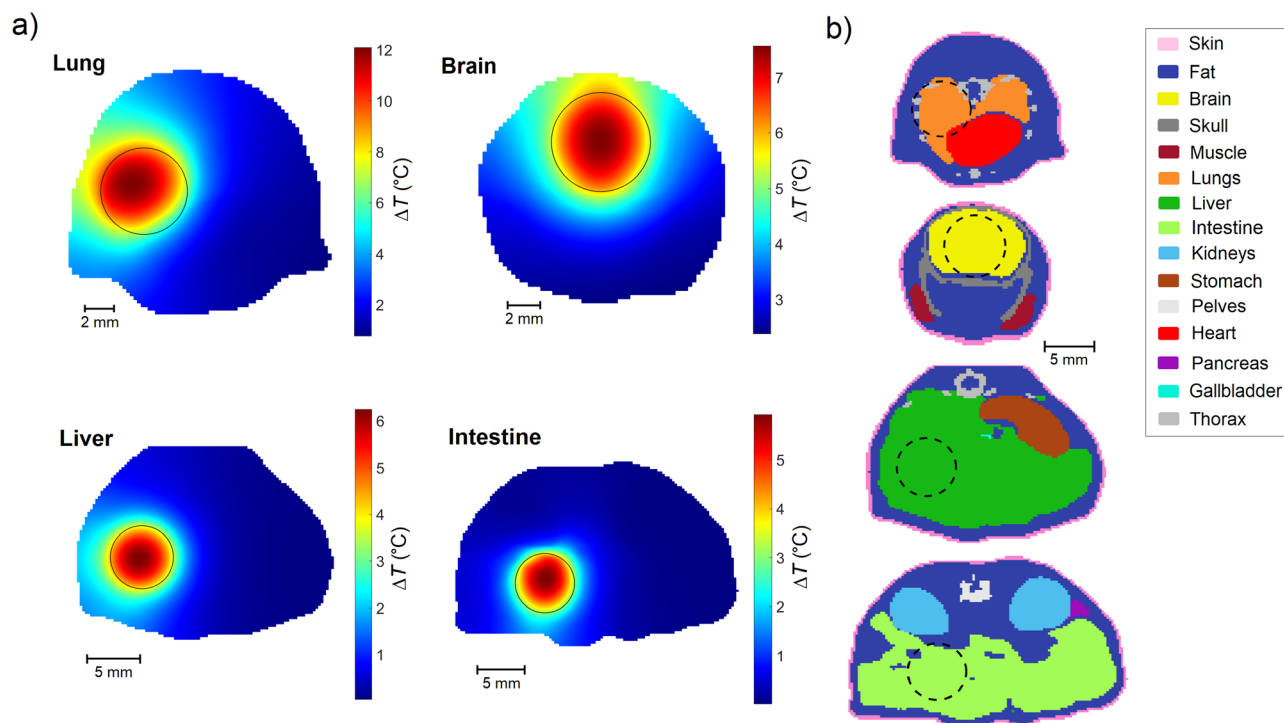


**Figure 7.** Analysis of thermal effects in a murine model. a) Maps of the temperature increase calculated on transverse sections of the mouse body in correspondence of the different target organs, setting the size of the target region (indicated with a black circle line) to 6 mm and the nanodisk dose to  $5 \text{ mg cm}^{-3}$ . b) Maps showing the tissues and organs traversed by the considered sections.

potential toxicity effects.<sup>[70]</sup> The maximum temperature increase is observed in the lung, due to the lower thermal conductivity and reduced blood perfusion rate, in comparison to the other considered organs (see Table 1). Overall, there is a variation in the order of 20–30% between the maximum and the average temperature increments, due to the thermal gradient from the center of the treated region to its periphery.

Another important aspect to be mentioned is the quite rapid heating transient, i.e., the thermal equilibrium is reached within 20 min at most, regardless of the organ where the target region is placed, its size  $\delta$  and the nanodisk dose. As illustrated in Figure 6c, for fixed values of  $\delta$  and nanodisk concentrations, the transient is longer in the lung, due to the higher heat capacity and reduced blood perfusion rate.

Finally, the temperature increase can show a non-spherical distribution when the target region extends toward other tissues or organs with significantly different thermal properties. This can lead to amplified side-effects and to a displacement of the point where the maximum temperature increment is reached, which moves from the region center toward tissues with lower thermal conductivity and blood perfusion rate. The above effects are observable in Figure 7a, which reports the maps of the temperature increase calculated on transverse sections of the mouse body placed in correspondence of the different target regions (see schematic in Figure 6a), fixing the size of the target region to 6 mm and the nanodisk dose to  $5 \text{ mg cm}^{-3}$ . The maps in Figure 7b show the tissues traversed by the considered sections. As an example, when the target region is mainly located in the lung, the maximum temperature increment shifts toward the thorax

and the surrounding fat, while close to the heart there is a more limited temperature increase. The temperature amplification effects due to the proximity to fat are found also for the liver and the intestine; for the brain there is a significant temperature increment toward the skull.

### 3. Conclusion

In this study, we have explored, with a numerical modeling based methodology, permalloy nanodisks for potential application in magnetic hyperthermia, as heating agents that produce heat via magnetic hysteresis. Modeling has proved to be fundamental to corroborate previous experimental results (from SLP measurements) and support nanodisk design, thus addressing bottom-up nanolithography process. The analysis has demonstrated that the optimal heating efficiency can be achieved with nanodisks having diameters around 100–200 nm and thickness of 20–30 nm. In this case, values of SLP in the order of  $500 \text{ W g}^{-1}$  can be obtained with field frequencies below 100 kHz, to avoid exceeding the Hergt–Dutz limit on the ac source parameters. The highest SLP ( $790 \text{ W g}^{-1}$ ) has been found at a field frequency of 75 kHz for a diameter of 100 nm and a thickness of 20 nm; this is a size that is also more advantageous in terms of cell uptake, blood circulation half-life and biodistribution. Moreover, for all the considered dimensions the nanodisks exhibit vortex state at remanence, thus conveniently reducing the possibility of aggregation.

Attention has been focused on phenomena that can influence the magnetization reversal process and consequently the hysteresis losses, at the basis of the heating mechanism. First,

we have analyzed the possible rotation of the nanodisks within low-viscosity media; under this condition, we have found that the alignment of the nanodisks with the applied field occurs very rapidly (order of milliseconds), leading to a condition for which the SLP is maximized. This result further corroborates previous experimental findings on ellipsoidal- or disk-shaped particles, for which an enhancement of the heating efficiency has been observed in water with respect to gel media or cell cultures. Second, we have investigated the influence of the inter-particle magnetostatic interactions, which result to play an important role at the nanoscale level, due to the possible formation of nanodisk clusters after the accumulation in the target tissue. Specifically, we have found that at very high local concentrations the magnetostatic interactions can be responsible for a reduction of 40–50% in the SLP, as a consequence of the strong modification of the shape of the global hysteresis loop. In particular, a gradual magnetization reversal process takes place, with indistinguishable vortex nucleation/expulsion transitions.

Finally, we have mimicked experimental tests, focusing on calorimetric measurements in test tubes and on in vivo applications in murine models. Via thermal simulations, we have demonstrated that in a mouse model temperature increments comparable to that obtained in calorimetric tests under quasi-adiabatic conditions can be achieved only by using an order of magnitude larger dosage of nanodisks, due to blood perfusion effects. In particular, a dose of at least  $5 \text{ mg cm}^{-3}$  of magnetic material is required to obtain a maximum temperature increase of some degrees centigrade in a 4 mm sized target region. When doubling the size of the target region we have found a significant enhancement of the maximum temperature increment, compatible with thermal ablation (e.g.,  $22.9^\circ \text{C}$  if the treated region is placed in the lung, characterized by low thermal conductivity and blood perfusion rate). This allows us the possibility of reducing the nanodisk dose for larger portions of tissue, with a consequent limitation of potential toxicity effects.

To conclude, another important aspect to be mentioned is the presence of side-effects at the periphery of the target region, with a significant temperature increase toward tissues with lower thermal conductivity and blood perfusion rate, like fat. This result demonstrates the utility of in silico models in supporting in vivo tests, with the prediction of possible adverse effects that can be partially controlled, for example, with a guided intra-tumoral particle injection.

Finally, as a future work we intend to implement a numerical model able to simulate the accumulation of the magnetic nanodisks inside the target tissue, in order to determine the induced temperature increase as a function of the nanodisk spatial and temporal distribution.

## 4. Experimental Section

**Hysteresis Loop Calculation:** The hysteresis loops of the permalloy nanodisks are calculated through the numerical integration of the LLG equation

$$\frac{\partial \mathbf{M}}{\partial t} = -\frac{\gamma}{(1 + \alpha^2)} \mathbf{M} \times \left[ \mathbf{H}_{\text{eff}} + \frac{\alpha}{M_S} (\mathbf{M} \times \mathbf{H}_{\text{eff}}) \right] \quad (1)$$

where  $\mathbf{M}$  is the magnetization vector with amplitude equal to the saturation magnetization  $M_S$ ,  $\gamma$  is the absolute value of the gyromagnetic ratio and  $\alpha$  is the damping coefficient. The effective field  $\mathbf{H}_{\text{eff}}$  is the sum of the applied external field, the magnetostatic field, the exchange field, and the magnetocrystalline anisotropy field, assumed to be negligible for permalloy. It can also include the thermal field  $\mathbf{H}_{\text{th}}$ , here evaluated following the Langevin approach and the fluctuation-dissipation theorem,<sup>[71]</sup> that is

$$\mathbf{H}_{\text{th}} = \boldsymbol{\eta}(\mathbf{r}, t) \sqrt{\frac{2\alpha k_B T}{\gamma \mu_0 M_S \Delta s^3 \Delta t}} \quad (2)$$

where  $T$  is the absolute temperature,  $k_B$  is the Boltzmann constant, and  $\mu_0$  is the magnetic permeability of vacuum. The components of stochastic vector  $\boldsymbol{\eta}$  are Gaussian random numbers, uncorrelated in space and time, and with zero mean value and dispersion 1. Parameter  $\Delta s$  is the average size of the spatial discretization, in the order of the exchange length ( $\approx 5 \text{ nm}$ ), and  $\Delta t$  is the time-step.

The numerical integration of the LLG equation is performed by means of a GPU-parallelized micromagnetic code, able to efficiently handle 3D random distributions of magnetostatically interacting magnetic thin-film objects.<sup>[41,72]</sup> The magnetization vector is assumed to be uniform within each discretization element. The exchange field is calculated with a finite difference technique able to treat non-structured hexahedral meshes, thus guaranteeing the accurate description of the nanodisk curved edges.<sup>[73]</sup> When many nanodisks are considered (as in the study of Sub-section 2.4), the magnetostatic field is separated into two contributions: an internal and an external one. The first contribution includes the magnetostatic interactions internal to each nanodisk and is determined by numerically solving the Green's integral equation. The second contribution describes the magnetostatic interactions between nanodisks and is calculated by approximating each nanodisk as a collection of magnetic dipoles, associated with mesh hexahedra.<sup>[41]</sup>

The time-integration of the LLG equation is performed by means of a norm-conserving scheme based on the Cayley transform and the Heun method.<sup>[74,75]</sup>

**Model of Mechanical Behavior in Fluids:** A simple physical model is used to analyze the temporal scale of the reorientation mechanisms occurring in fluids, where the magnetic nanodisks tend to align with the applied alternating field. We build an orthogonal system of reference with center in the nanodisk barycentre and axes that coincide with the projection of the field on the nanodisk plane ( $u$ ), the fixed axis of rotation ( $w$ ) and the normal to the nanodisk plane ( $v$ ). The model, based on the angular momentum conservation equation, aims at determining the time evolution of the rotation angle  $\theta$ , identified as the angle between  $v$ -axis and the direction of the field, or its complementary angle  $\varphi$ , i.e. the angle between the field direction and  $u$ -axis (see schematic below Figure 3a). The equation for the nanodisk angular motion in a fluid in the presence of an external magnetic field  $\mathbf{H}_a$  can be written in the following form:

$$I \frac{d\boldsymbol{\omega}}{dt} = \mu_0 (\mathbf{m} \times \mathbf{H}_a) + \boldsymbol{\tau}_D + \boldsymbol{\tau}_B \quad (3)$$

where  $I$  is the moment of inertia of the nanodisk,  $\boldsymbol{\omega} = \frac{d\theta}{dt} \hat{\mathbf{w}}$  is its angular velocity,  $\mathbf{m}$  is its magnetic moment,  $\boldsymbol{\tau}_D$  is the dynamic drag torque, and  $\boldsymbol{\tau}_B$  is the Brownian torque. The latter is described as a Gaussian white noise following the Langevin approach and the fluctuation-dissipation theorem.<sup>[76]</sup>

The dynamic drag torque is expressed as  $\boldsymbol{\tau}_D = -\nu \boldsymbol{\Omega}_R \cdot \boldsymbol{\omega}$ , where  $\nu$  is the fluid viscosity and the rotation tensor  $\boldsymbol{\Omega}_R$  depends on the shape of the particle and on its center of rotation. For a thin homogeneous disk rotating around its center of mass  $\boldsymbol{\Omega}_R = \mathbf{I} \frac{32}{3} d^2$ , where  $\mathbf{I}$  is the identity  $3 \times 3$  matrix and  $d$  is the disk diameter.<sup>[77]</sup>

Regarding magnetic torque, the nanodisk is approximated as a magnetic dipole whose moment  $\mathbf{m}$  is a function of  $\mathbf{H}_a(t)$ , and is obtained by volume averaging the magnetization spatial distribution, obtained from micromagnetic simulations of nanodisks orientated at different angles  $\varphi$ , under different field conditions.



**Simulation of Thermal Effects in Test Tubes:** To simulate the thermal effects induced in fluids contained in test tubes, we have implemented a 3D finite element code that solves the heat transfer equation under the hypothesis of negligible convection phenomena. This results in

$$\rho(\mathbf{r}) C_p(\mathbf{r}) \frac{\partial T(\mathbf{r}, t)}{\partial t} = \nabla \cdot k \nabla T(\mathbf{r}, t) + \Gamma(\mathbf{r}) Q_{\text{MNDs}}(\mathbf{r}, t) \quad (4)$$

where  $T$  is the temperature,  $\rho$  is the material density,  $C_p$  is the material heat capacity,  $k$  is the material thermal conductivity,  $Q_{\text{MNDs}}$  is the heating power produced by the magnetic nanodisks per unit volume and function  $\Gamma$  is equal to 1 in the particle-fluid suspension region and zero elsewhere.<sup>[78]</sup> Equation (4) is completed by the following boundary condition on the test tube exterior surface  $\partial\Omega$ :

$$q = -k \frac{\partial T}{\partial n} = -h(T_{\text{ext}} - T) \quad \text{on } \partial\Omega \quad (5)$$

where  $q$  is the outward heat flux,  $T_{\text{ext}}$  is the external temperature (far away from the modeled domain) and  $h$  is the heat transfer coefficient, which takes into account exterior convective cooling. At the initial time instant ( $t = 0$ ),  $T = T_{\text{ext}}$ .

The finite element solution is obtained by discretizing the domain under analysis into a tetrahedral mesh and by using linear shape functions. The time integration is performed with a Crank–Nicholson's method.

**In Silico Simulation of Thermal Effects:** To simulate the hyperthermia effects induced in living tissues, we have implemented a 3D finite element code that solves the Pennes' bioheat transfer equation, namely

$$\rho(\mathbf{r}) C_p(\mathbf{r}) \frac{\partial T(\mathbf{r}, t)}{\partial t} = \nabla \cdot k \nabla T(\mathbf{r}, t) + \Gamma(\mathbf{r}) Q_{\text{MNDs}}(\mathbf{r}, t) + Q_m - W C_{\text{blood}}(T(\mathbf{r}, t) - T_{\text{blood}}) \quad (6)$$

where  $T$  is the local tissue temperature,  $T_{\text{blood}}$  is the arterial temperature,  $\rho$  is the tissue density,  $C_p$  is the tissue heat capacity,  $k$  is the tissue thermal conductivity,  $Q_{\text{MNDs}}$  is the heating power produced by the magnetic nanodisks per unit volume and function  $\Gamma$  is equal to 1 in the portion of tissue where the magnetic nanodisks are dispersed (target region),  $Q_m$  is the metabolic heat generation rate per unit volume,  $C_{\text{blood}}$  is the heat capacity of blood, fixed to  $3617 \text{ J kg}^{-1} \text{ K}^{-1}$ , and  $W$  is the local tissue-blood perfusion rate.<sup>[64,79]</sup>

Equation (6) is completed by the following boundary condition at the interface  $\partial\Omega$  between skin and air:

$$q = -k \frac{\partial T}{\partial n} = -h(T_{\text{air}} - T_{\text{skin}}) \quad \text{on } \partial\Omega, \quad (7)$$

where  $q$  is the outward heat flux,  $T_{\text{air}}$  is the air temperature,  $T_{\text{skin}}$  is the skin temperature and  $h$  is the heat convection coefficient between the skin surface and the surrounding air under physiologically basal state and is an overall contribution from natural convection and radiation. The initial condition (at  $t = 0$ ) corresponds to the steady-state temperature distribution before heating, governed by the metabolic heat.

The spatial and time discretization of Equation (6) is performed with the same methodology described for Equation (4).

## Acknowledgements

The work here presented is developed in the framework of the 18HLT06 RaChy Joint Research Project that received funding from the European Metrology Programme for Innovation and Research (EMPIR) Program, co-financed by the Participating States, and from the European Union's Horizon 2020 Research and Innovation Program.

## Conflict of Interest

The authors declare no conflict of interest.

## Data Availability Statement

The data that support the findings of this study are available from the corresponding author upon reasonable request.

## Keywords

bioheat modeling, magnetic hyperthermia, magnetic nanodisks, micro-magnetic modeling, nanomedicine

Received: January 29, 2021  
Published online: March 26, 2021

- [1] V. Uhlř, M. Urbánek, L. Hladík, J. Spousta, M.-Y. Im, P. Fischer, N. Eibagi, J. J. Kan, E. E. Fullerton, T. Šikola, *Nat. Nanotechnol.* **2013**, *8*, 341.
- [2] H. Jung, Y.-S. Choi, K.-S. Lee, D.-S. Han, Y.-S. Yu, M.-Y. Im, P. Fischer, S.-K. Kim, *ACS Nano* **2012**, *6*, 3712.
- [3] R. Hertel, *Nat. Nanotechnol.* **2013**, *8*, 318.
- [4] V. S. Pribyl, I. N. Krivorotov, G. D. Fuchs, P. M. Braganca, O. Ozatay, J. C. Sankey, D. C. Ralph, R. A. Buhrman, *Nat. Phys.* **2007**, *3*, 498.
- [5] A. Manzin, R. Ferrero, *Appl. Phys. Lett.* **2019**, *115*, 042402.
- [6] M. Goiriena-Goikoetxea, D. Muñoz, I. Orue, M. L. Fernández-Gubieda, J. Bokor, A. Muela, A. García-Arribas, *Appl. Phys. Rev.* **2020**, *7*, 011306.
- [7] L. Peixoto, R. Magalhães, D. Navas, S. Moraes, C. Redondo, R. Morales, J. P. Araújo, C. T. Sousa, *Appl. Phys. Rev.* **2020**, *7*, 011310.
- [8] A. G. Roca, L. Gutiérrez, H. Gavilán, M. E. Fortes Brollo, S. Veintemillas-Verdaguer, M. del Puerto Morales, *Adv. Drug Delivery Rev.* **2019**, *138*, 68.
- [9] R. M. Fratila, S. Rivera-Fernández, J. M. de la Fuente, *Nanoscale* **2015**, *7*, 8233.
- [10] V. Clavijo-Jordan, V. D. Kodibagkar, S. C. Beeman, B. D. Hann, K. M. Bennett, *Wiley Interdiscip. Rev.: Nanomed. Nanobiotechnol.* **2012**, *4*, 345.
- [11] X. Zhu, C. Vo, M. Taylor, B. R. Smith, *Mater. Horiz.* **2019**, *6*, 1094.
- [12] J. Dulińska-Litewka, A. Łazarczyk, P. Hałubiec, O. Szafranski, K. Kar-nas, A. Karewicz, *Materials* **2019**, *12*, 617.
- [13] Y. Xiao, J. Du, *J. Mater. Chem. B* **2020**, *8*, 354.
- [14] D.-H. Kim, E. A. Rozhkova, I. V. Ulasov, S. D. Bader, T. Rajh, M. S. Lesniak, V. Novosad, *Nat. Mater.* **2010**, *9*, 165.
- [15] S. Leulmi, X. Chauchet, M. Morcrette, G. Ortiz, H. Joisten, P. Sabon, T. Livache, Y. Hou, M. Carrière, S. Lequienabh, B. Dieny, *Nanoscale* **2015**, *7*, 15904.
- [16] H. Chiriac, E. Radu, M. Ţibu, G. Stoian, G. Ababei, L. Lăbuşcă, D.-D. Herea, N. Lupu, *Sci. Rep.* **2018**, *8*, 11538.
- [17] Y. Cheng, M. E. Muroski, D. C. M. C. Petit, R. Mansell, T. Vemulkar, R. A. Morshed, Y. Han, I. V. Balyasnikova, C. M. Horbinski, X. Huang, L. Zhang, R. P. Cowburn, M. S. Lesniak, *J. Controlled Release* **2016**, *223*, 75.
- [18] M. E. Muroski, R. A. Morshed, Y. Cheng, T. Vemulkar, R. Mansell, Y. Han, L. Zhang, K. S. Aboody, R. P. Cowburn, M. S. Lesniak, *PLoS One* **2016**, *11*, e0145129.
- [19] D.-H. Kim, P. Karavayev, E. A. Rozhkova, J. Pearson, V. Yefremenko, S. D. Baderac, V. Novosad, *J. Mater. Chem.* **2011**, *21*, 8422.
- [20] V. E. Orel, M. Tselepi, T. Mitrelias, A. Rykhalskiy, A. Romanov, V. B. Orel, A. Shevchenko, A. Burlaka, S. Lukin, C. H. W. Barnes, *Nanomedicine* **2018**, *14*, 1249.
- [21] M. Zhang, C. M. Earhart, C. Ooi, R. J. Wilson, M. Tang, S. X. Wang, *Nano Res.* **2013**, *6*, 745.
- [22] M. Albert, M. Beg, D. Chernyshenko, M.-A. Bisotti, R. L. Carey, H. Fangohr, P. J. Metaxas, *Nanotechnology* **2016**, *27*, 455502.

- [23] B. T. Mai, P. B. Balakrishnan, M. J. Barthel, F. Piccardi, D. Niculaes, F. Marinaro, S. Fernandes, A. Curcio, H. Kakwere, G. Autret, R. Cingolani, F. Gazeau, T. Pellegrino, *ACS Appl. Mater. Interfaces* **2019**, *11*, 5727.
- [24] R. Di Corato, A. Espinosa, L. Lartigue, M. Tharaud, S. Chat, T. Pellegrino, C. Ménager, F. Gazeau, C. Wilhelm, *Biomaterials* **2014**, *35*, 6400.
- [25] K. Simeonidis, M. P. Morales, M. Marciello, M. Angelakeris, P. de la Presa, A. Lazaro-Carrillo, A. Tabero, A. Villanueva, O. Chubykalo-Fesenko, D. Serantes, *Sci. Rep.* **2016**, *6*, 38382.
- [26] Y. Yang, X. Liu, Y. Lv, T. S. Heng, X. Xu, W. Xia, T. Zhang, J. Fang, W. Xiao, J. Ding, *Adv. Funct. Mater.* **2015**, *25*, 812.
- [27] N. A. Usov, M. S. Nesmeyanov, V. P. Tarasov, *Sci. Rep.* **2018**, *8*, 1224.
- [28] X. L. Liu, Y. Yang, C. T. Ng, L. Y. Zhao, Y. Zhang, B. H. Bay, H. M. Fan, J. Ding, *Adv. Mater.* **2015**, *27*, 1939.
- [29] C. S. B. Dias, T. D. M. Hanchuk, H. Wender, W. T. Shigeyosi, J. Kobarg, A. L. Rossi, M. N. Tanaka, M. B. Cardoso, F. Garcia, *Sci. Rep.* **2017**, *7*, 14843.
- [30] D. W. Wong, W. L. Gan, Y. K. Teo, W. S. Lew, *Nanoscale Res. Lett.* **2019**, *14*, 376.
- [31] C. Martinez-Boubeta, K. Simeonidis, A. Makridis, M. Angelakeris, O. Iglesias, P. Guardia, A. Cabot, L. Yedra, S. Estradé, F. Peiró, Z. Saghi, P. A. Midgley, I. Conde-Leborán, D. Serantes, D. Baldomir, *Sci. Rep.* **2013**, *3*, 1038.
- [32] R. Ferrero, A. Manzin, G. Barrera, F. Celegato, M. Coisson, P. Tiberto, *Sci. Rep.* **2019**, *9*, 6591.
- [33] K. Maier-Hauff, R. Rothe, R. Scholz, U. Gneveckow, P. Wust, B. Thiesen, A. Feussner, A. von Deimling, N. Waldoefner, R. Felix, A. Jordan, *J. Neuro-Oncol.* **2007**, *81*, 53.
- [34] S. Laurent, S. Dutz, U. O. Häfeli, M. Mahmoudi, *Adv. Colloid Interface Sci.* **2011**, *166*, 8.
- [35] X. Liu, Y. Zhang, Y. Wang, W. Zhu, G. Li, X. Ma, Y. Zhang, S. Chen, S. Tiwari, K. Shi, S. Zhang, H. Ming Fan, Y. Xiang Zhao, X.-J. Liang, *Theranostics* **2020**, *10*, 3793.
- [36] K. D. Bakoglidis, K. Simeonidis, D. Sakellari, G. Stefanou, M. Angelakeris, *IEEE Trans. Magn.* **2012**, *48*, 1320.
- [37] M. Jeun, S. Lee, J. K. Kang, A. Tomitaka, K. W. Kang, Y. H. Kim, Y. Takemura, K.-W. Chung, J. Kwak, S. Bae, *Appl. Phys. Lett.* **2012**, *100*, 3.
- [38] R. Hergt, S. Dutz, *J. Magn. Magn. Mater.* **2007**, *311*, 187.
- [39] W. J. Atkinson, I. A. Brezovich, D. P. Chakraborty, *IEEE Trans. Biomed. Eng.* **1984**, *31*, 70.
- [40] G. Barrera, L. Serpe, F. Celegato, M. Coisson, K. Martina, R. Canaparo, P. Tiberto, *Interface Focus* **2016**, *6*, 20160052.
- [41] A. Manzin, R. Ferrero, *J. Magn. Magn. Mater.* **2019**, *492*, 165649.
- [42] J. K. Ha, R. Hertel, J. Kirschner, *Phys. Rev. B* **2003**, *67*, 224432.
- [43] C. Luo, Y. Fu, D. Zhang, S. Yuan, Y. Zhai, S. Dong, H. Zhai, *J. Magn. Magn. Mater.* **2015**, *374*, 711.
- [44] J. Tejada, B. Martinez, A. Labarta, R. Grossinger, H. Sassik, M. Vazquez, A. Hernando, *Phys. Rev. B* **1990**, *42*, 898.
- [45] Z. Nemat, S. M. Salili, J. Alonso, A. Ataie, R. Das, M. H. Phan, H. Srikanth, *J. Alloys Compd.* **2017**, *714*, 709.
- [46] M. Ma, Y. Zhang, Z. Guo, N. Gu, *Nanoscale Res. Lett.* **2013**, *8*, 16.
- [47] S. Dutz, M. Kettering, I. Hilger, R. Müller, M. Zeisberger, *Nanotechnology* **2011**, *22*, 265102.
- [48] Y.-F. Wu, P.-S. Hsu, C.-S. Tsai, P.-C. Pan, Y.-L. Chen, *Sci. Rep.* **2018**, *8*, 7173.
- [49] S. M. Moghimi, D. Simberg, *J. Nanopart. Res.* **2018**, *20*, 169.
- [50] S. Sindhvani, A. M. Syed, J. Ngai, B. R. Kingston, L. Maiorino, J. Rothschild, P. MacMillan, Y. Zhang, N. Unni Rajesh, T. Hoang, J. L. Y. Wu, S. Wilhelm, A. Zilman, S. Gadde, A. Sulaiman, B. Ouyang, Z. Lin, L. Wang, M. Egeblad, W. C. W. Chan, *Nat. Mater.* **2020**, *19*, 566.
- [51] K. Yaehne, A. Tekrony, A. Clancy, Y. Gregoriou, J. Walker, K. Dean, T. Nguyen, A. Doiron, K. Rinker, X. Y. Jiang, S. Childs, D. Cramb, *Small* **2013**, *9*, 3118.
- [52] M. T. Matter, J.-H. Li, I. Lese, C. Schreiner, L. Bernard, O. Scholder, J. Hubeli, K. Keevend, E. Tzolaki, E. Bertero, S. Bertazzo, R. Zboray, R. Olariu, M. A. Constantinescu, R. Figi, I. K. Herrmann, *Adv. Sci.* **2020**, *7*, 2000912.
- [53] S. Sindhvani, A. M. Syed, S. Wilhelm, D. R. Glancy, Y. Y. Chen, M. Dobosz, W. C. W. Chan, *ACS Nano* **2016**, *10*, 5468.
- [54] H. Dähling, J. Grandke, U. Teichgräber, I. Hilger, *Mol. Imaging Biol.* **2015**, *17*, 763.
- [55] M. Vicentini, R. Ferrero, A. Manzin, *J. Magn. Magn. Mater.* **2020**, *513*, 167234.
- [56] H. B. Frieboes, M. Wu, J. Lowengrub, P. Decuzzi, V. Cristini, *PLoS One* **2013**, *8*, e56876.
- [57] H. A. Albarqi, L. H. Wong, C. Schumann, F. Y. Sabei, T. Korzun, X. Li, M. N. Hansen, P. Dhagat, A. S. Moses, O. Taratula, O. Taratula, *ACS Nano* **2019**, *13*, 6383.
- [58] C. Haase, U. Nowak, *Phys. Rev. B* **2012**, *85*, 045435.
- [59] C. Guibert, V. Dupuis, V. Peyre, J. Fresnais, *J. Phys. Chem. C* **2015**, *119*, 28148.
- [60] R. R. Wildeboer, P. Southern, Q. A. Pankhurst, *J. Phys. D: Appl. Phys.* **2014**, *47*, 495003.
- [61] A. Makridis, S. Curto, G. C. van Rhoon, T. Samaras, M. Angelakeris, *J. Phys. D: Appl. Phys.* **2019**, *52*, 255001.
- [62] E. A. Périgo, G. Hemery, O. Sandre, D. Ortega, E. Garaio, F. Plazaola, F. J. Teran, *Appl. Phys. Rev.* **2015**, *2*, 041302.
- [63] B. Dogdas, D. Stout, A. F. Chatzioannou, R. M. Leahy, *Phys. Med. Biol.* **2007**, *52*, 577.
- [64] <https://itis.swiss/virtual-population/tissue-properties/overview/> (accessed: February 2021).
- [65] S. Kodera, A. Hirata, *Int. J. Environ. Res. Public Health* **2018**, *15*, 2320.
- [66] C. J. Gordon, *Physiol. Behav.* **2017**, *179*, 55.
- [67] S. Kossatz, R. Ludwig, H. Dähling, V. Ettelt, G. Rimkus, M. Marciello, G. Salas, V. Patel, F. J. Teran, I. Hilger, *Pharm. Res.* **2014**, *31*, 3274.
- [68] A. Attaluri, R. Ma, Y. Qiu, W. Li, L. Zhu, *Int. J. Hyperthermia* **2011**, *27*, 491.
- [69] F. Oltolina, A. Peigneux, D. Colangelo, N. Clemente, A. D'Urso, G. Valente, G. R. Iglesias, C. Jiménez-Lopez, M. Prat, *Cancers* **2020**, *12*, 2564.
- [70] B. Kozissnik, A. C. Bohorquez, J. Dobson, C. Rinaldi, *Int. J. Hyperthermia* **2013**, *29*, 706.
- [71] E. Martínez, L. López-Díaz, L. Torres, C. J. García-Cervera, *J. Phys. D: Appl. Phys.* **2007**, *40*, 942.
- [72] O. Bottauscio, A. Manzin, *J. Appl. Phys.* **2014**, *115*, 17D122.
- [73] O. Bottauscio, A. Manzin, *IEEE Trans. Magn.* **2012**, *48*, 3250.
- [74] O. Bottauscio, A. Manzin, *IEEE Trans. Magn.* **2011**, *47*, 1154.
- [75] A. Manzin, O. Bottauscio, *J. Appl. Phys.* **2010**, *108*, 093917.
- [76] M. N. Romodina, E. V. Lyubin, A. A. Fedyanin, *Sci. Rep.* **2016**, *6*, 21212.
- [77] H. Brenner, *Chem. Eng. Sci.* **1963**, *18*, 1.
- [78] A. M. M. Gherman, S. Boca, A. Vulpoi, M. V. Cristea, C. Farcau, V. Tosa, *Nanotechnology* **2020**, *31*, 125701.
- [79] M. A. Giordano, G. Gutierrez, C. Rinaldi, *Int. J. Hyperthermia* **2010**, *26*, 475.